Acta Oceanol. Sin., 2021, Vol. 40, No. 3, P. 122–133
https://doi.org/10.1007/s13131-021-1712-7
http://www.hyxb.org.cn
E-mail: hyxbe@263.net

Sea surface temperature retrieval based on simulated microwave polarimetric measurements of a one-dimensional synthetic aperture microwave radiometer

Mengyan Feng[1], Weihua Ai[1]*, Wen Lu[1], Chengju Shan[2], Shuo Ma[1], Guanyu Chen[3]

[1] College of Meteorology and Oceanography, National University of Defense Technology, Nanjing 211101, China

[2] Zhejiang University of Water Resources and Electric Power, Hangzhou 310000, China

[3] PLA Troop 32033, Haikou 570100, China

Received 9 April 2020; accepted 3 June 2020

Abstract

Compared with traditional real aperture microwave radiometers, one-dimensional synthetic aperture microwave radiometers have higher spatial resolution. In this paper, we proposed to retrieve sea surface temperature using a one-dimensional synthetic aperture microwave radiometer that operates at frequencies of 6.9 GHz, 10.65 GHz, 18.7 GHz and 23.8 GHz at multiple incidence angles. We used the ERA5 reanalysis data provided by the European Centre for Medium-Range Weather Forecasts and a radiation transmission forward model to calculate the model brightness temperature. The brightness temperature measured by the spaceborne one-dimensional synthetic aperture microwave radiometer was simulated by adding Gaussian noise to the model brightness temperature. Then, a backpropagation (BP) neural network algorithm, a random forest (RF) algorithm and two multiple linear regression algorithms (RE1 and RE2) were developed to retrieve sea surface temperature from the measured brightness temperature within the incidence angle range of 0°–65°. The results show that the retrieval errors of the four algorithms increase with the increasing Gaussian noise. The BP achieves the lowest retrieval errors at all incidence angles. The retrieval error of the RE1 and RE2 decrease first and then increase with the incidence angle and the retrieval error of the RF is contrary to that of RE1 and RE2.

Key words: one-dimensional synthetic aperture microwave radiometer, sea surface temperature retrieval, neural network, random forest, multiple linear regression

Citation: Feng Mengyan, Ai Weihua, Lu Wen, Shan Chengju, Ma Shuo, Chen Guanyu. 2021. Sea surface temperature retrieval based on simulated microwave polarimetric measurements of a one-dimensionalsynthetic aperture microwave radiometer. Acta Oceanologica Sinica, 40(3): 122–133, doi: 10.1007/s13131-021-1712-7

1 Introduction

Sea surface temperature (SST) is an important parameter to understand air-sea interactions and climate change (Alsweiss et al., 2017). It plays a significant role in the hydrological cycle and energy cycle, and it is closely related to the formation of El Niño, La Niña and typhoons (Emanuel, 1999; Martin-Neira et al., 1994; McClain et al., 1985; McPhaden, 1999). Therefore, it is important to obtain high-quality sea surface temperature data.

Many conventional methods such as measurements from ship and marine buoys cannot obtain large-scale and long-term sea surface temperature data. Therefore, satellite remote sensing data are used to derive global sea surface temperature. Compared with infrared remote sensing, microwave remote sensing can pass through the clouds (Ulaby et al., 1983; Chelton and Wentz, 2005; Mätzler, 2006). It can observe sea surface temperature during the entire day and in all weather conditions.

At present, in-orbit microwave radiometers such as the WindSat, AMSR-2 and TMI, are conically scanning real aperture microwave radiometer imagers. They have only one incidence angle. The WindSat and AMSR-2 radiometers include C-band, which has the highest sensitivity to sea surface temperature. However, real aperture microwave radiometers suffer from inherent limitations concerning their wavelength and antenna, leading to a low spatial resolution. For example, the spatial resolution of the C-band is approximately 50 km. Although increasing the size of the antenna can improve the spatial resolution, it also increases the volume and quality of the radiometer (Kilic et al., 2018).

Compared with traditional real aperture microwave radiometers, synthetic aperture microwave radiometers have higher spatial resolution and multiple incidence angles. The principle of synthetic aperture microwave radiometers is to use a small aperture antenna array instead of a large real aperture antenna. The cross-correlating of the signals from pairs of antennas is measured at many different baselines. Each baseline yields a sample point in the Fourier transform of the brightness temperature map of the scene, and the brightness temperature images are reconstructed after all measurements are completed by inverting the transform. The spatial resolution is determined by spectrum sampling, not by the size of antennas (Le Vine, 1990; Camps et al., 2016). It is similar in principle to earth rotation synthesis employed in radio astronomy (Ruf et al., 1988; Schanda, 1979).

Recently, the spaceborne synthetic aperture microwave radiometer has been successfully applied only in the remote sensing of salinity. The Microwave Imaging Radiometer using

Foundation item: The National Natural Science Foundation of China under contract Nos 41475019 and 41705007.
*Corresponding author, E-mail: a1044175130@163.com

Aperture Synthesis (MIRAS) instrument mounted on board the Soil Moisture and Ocean Salinity (SMOS) satellite is a two-dimensional synthetic aperture microwave radiometer. It operates at the L-band, which is sensitive to salinity (Martin-Neira et al., 1994, 2002). However, two-dimensional synthetic aperture microwave radiometers have the disadvantages of complex imaging methods and difficult calibration. In contrast, the systematic complexity of one-dimensional synthetic aperture microwave radiometers is greatly reduced (Le Vine et al., 1990, 1994); thus, it is easy to achieve high spatial resolution detection (Le Vine et al., 1990).

Currently, the one-dimensional synthetic aperture microwave radiometer has only been used for airborne and ground-based observation experiments (Le Vine et al., 1994, 2001). To retrieve sea surface temperature by one-dimensional synthetic aperture microwave radiometers from space, we propose a one-dimensional synthetic aperture microwave radiometer operate at frequencies of 6.9 GHz, 10.65 GHz, 18.7 GHz, and 23.8 GHz. Each frequency adopts a dual polarization observation mode. Since there is no one-dimensional synthetic aperture microwave radiometer in orbit, in this paper, a radiation transmission forward model is used to simulate the brightness temperature measured by the spaceborne one-dimensional synthetic aperture microwave radiometer. The concept of one-dimensional synthetic aperture microwave radiometer is shown in Fig. 1.

At present, the sea surface temperature retrieval algorithms for microwave remote sensing mainly include physical algorithms and empirical algorithms. The physical basis for the physical algorithms are the radiative transfer model. It retrieve sea surface temperature by establishing a cost function of observations and model simulations (Meissner and Wentz, 2005; Konер et al., 2015). For example, both AMSR (Wentz and Meissner, 2000) and WindSat (Bettenhausen et al., 2006; Brown et al., 2006) use physical algorithms. Empirical algorithms include the D-Matrix algorithm (Goodberlet et al., 1990), linear regression algorithm (Wentz and Meissner, 2000) and neural network method (Obligis et al., 2005; Krasnopolsky et al., 2000), which establish an empirical relationship between brightness temperature and sea surface temperature. However, these algorithms cannot be used directly for the one-dimensional synthetic aperture microwave radiometer because it includes multiple incidence angles. In this paper, we mainly study empirical algorithms and propose two machine learning algorithms (backpropagation neural network and random forest) and two multiple linear regression algorithms to retrieve sea surface temperature.

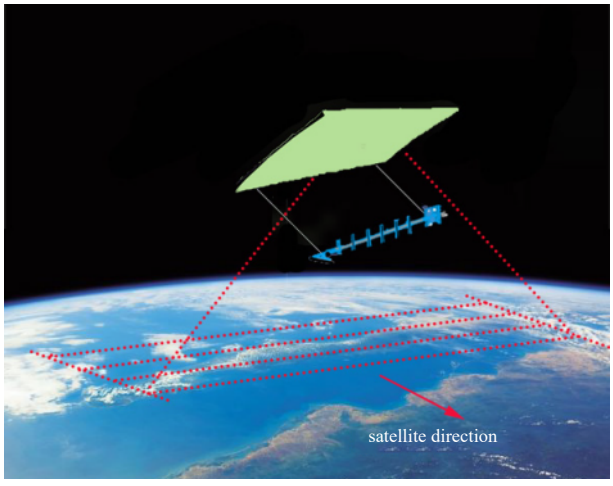

Fig. 1. The concept of one-dimensional synthetic aperture microwave radiometer.

The rest of this paper is organized as follows. Section 2 introduces the parameters of the one-dimensional synthetic aperture microwave radiometer, and Section 3 presents the methods and data. The methods include the radiation transmission forward model and retrieval method. The results and analyses are discussed in Section 4, and the conclusions are drawn in Section 5.

2 Introduction of a one-dimensional synthetic aperture microwave radiometer

The synthetic aperture radiometer imaging is an indirect method to measure the brightness temperature of a scene. It measures the spatial frequency component of the scene by measuring all of the coherent products of the output voltage from pairs of antennas (Le Vine, 1990), which are called visibility functions (Corbella et al., 2004), the brightness temperature image is obtained by an inverse Fourier transform.

In the one-dimensional synthetic aperture microwave radiometer, the frequencies are 6.9 GHz, 10.65 GHz, 18.7 GHz and 23.8 GHz, and every frequency operates at vertical and horizontal polarization. Moreover, 6.9 GHz is the most significant frequency because the sensitivity of 6.9 GHz to sea surface temperature is high. Table 1 lists some parameters of 6.9 GHz.

According to the positions of the antenna elements, we define the minimum wavelength spacing between antenna elements to be 0.73λ, and the maximum distance is $183\times0.73\lambda$, where λ is the wavelength. According to Lim's study (Lim, 2009), the angular resolution is $\Delta\theta\approx1/(183\times0.73\lambda)$, which provides an angular resolution of approximately 0.43°. The parabolic cylindrical antenna has a size of 12 m×10 m, and all small antenna elements share a parabolic cylindrical antenna. We assume that the satellite is operating along a track at an altitude of 900 km. At nadir, the spatial resolution can be calculated at approximately 5 km by

$$\Delta x \approx 1.2\frac{\lambda}{D}H, \tag{1}$$

where Δx is spatial resolution, D is the size of the parabolic antenna and H is the height of the satellite orbit.

Figure 2 shows the schematic diagram of the incidence angle of a spaceborne one-dimensional synthetic aperture radiometer.

According to the curvature of the earth, satellite height and angular range of the field of view, we can calculate the incidence angles as $-51°\leqslant\theta\leqslant51°$. The equations are as follows:

$$L=(R_e+H)\cos\beta-\sqrt{R_e^2-(R_e+H)^2(1-\cos^2\beta)}, \tag{2}$$

$$\theta=\pi-\arccos\left[\frac{L^2+R_e^2-(R_e+H)^2}{2LR_e}\right], \tag{3}$$

where β is the field of view of the one-dimensional synthetic aperture microwave radiometer, H is the orbital height, R_e is the radius of the earth, and L is the distance from the spaceborne one-dimensional synthetic aperture microwave radiometer to the observation scene.

When the spaceborne one-dimensional synthetic aperture microwave radiometer observes the earth, the vertical polarization and horizontal polarization observation modes work alternately. The antenna elements of all frequencies have the same spatial resolution.

Table 1. Parameters of the one-dimensional synthetic aperture radiometer

Parameter	Values
Frequency/GHz	6.9
Bandwidth/MHz	200
Polarization modes	vertical and horizontal polarization
Integral time/s	0.5
Number of antenna elements	55
Minimum spacing between antenna elements	0.73λ
Angular range of the field of view	–43° to 43°
Angular resolution	0.43°
Antenna element positions	[0 1 2 3 7 11 12 14 21 24 26 28 38 43 58 59 60 65 68 70 73 75 76 78 83 86 88 93 101 103 105 112 118 121 122 123 132 133 134 137 147 148 153 156 164 166 172 173 174 175 178 180 181 182 183]
Parabolic size	12 m×10 m
Spatial resolution at nadir/km	5
Range of incidence angle θ with vertical observation	–51° to 51°

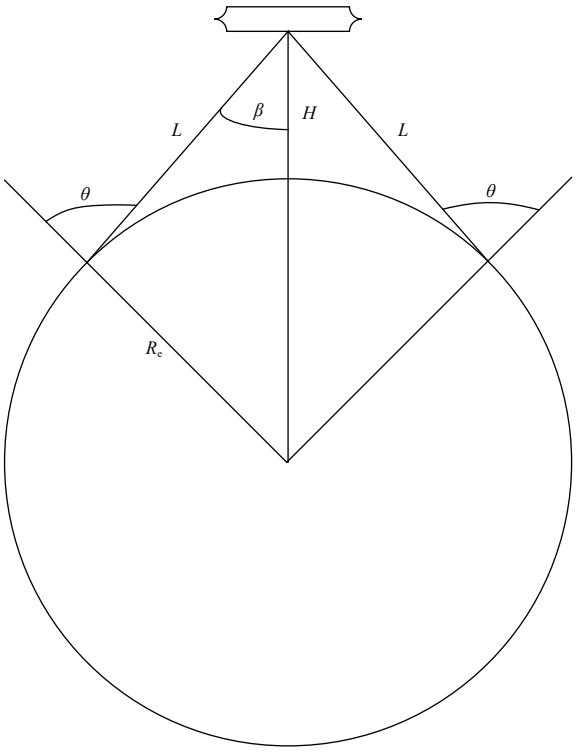

Fig. 2. The schematic diagram of the incidence angle of a one-dimensional synthetic aperture radiometer.

3 Data and methods

3.1 *Data*

In this paper, the newest version of the European Centre for Medium-Range Weather Forecasts (ECMWF) reanalysis data, ERA5, is used to calculate the model brightness temperature with the radiation transmission forward model. The data acquisition times are 0:00 and 12:00 on January 15, April 15, July 15, and October 15, 2018. The data contain the 10-m wind speed components u and v, total column cloud liquid water content L, total column water vapor content V, average rainfall rate R and sea surface temperature T_S. The spatial resolution of the data is 0.25°. We calculate the wind speed W and wind direction φ using the 10-m wind speed components u and v. The data under precipitation conditions $R>0$, $T_S<271.15$ conditions and unreasonable data $L<0$ are eliminated. Since the seawater salinity S has little effect on the frequencies of the one-dimensional synthetic aperture microwave radiometer, we set the seawater salinity to 35.

We obtain approximately 730 000 sets of data after processing. Statistical histograms of the sea surface temperature, wind direction, wind speed, total column cloud liquid water content and total column water vapor content are shown in Fig. 3. Finally, we divide the data into a training set and a test set on average. The training set is used to train the retrieval algorithm, and the test set is used to test the performance of the retrieval algorithm.

3.2 *Radiation transmission forward model*

The brightness temperature $T_{B,p}$ received by the spaceborne one-dimensional synthetic aperture microwave radiometer can be expressed as follows (Meissner and Wentz, 2009, 2012):

$$\begin{cases} T_{B,p} = T_{BU} + \tau E_p T_S + \tau T_{B\Omega} \\ T_{B\Omega} = R_p \left(T_{BD} + \tau T_{cold}\right) + T_{B,scat,p} \\ T_{B,scat,p} = \Omega_p \left(\tau, W\right) \left(T_{BD} + \tau T_{cold} - T_{cold}\right) R_p \end{cases}, \tag{4}$$

where the subscript p denotes the polarization mode, p means v or h, represents vertical or horizantal polorization T_{BU} and T_{BD} are the upwelling and downwelling atmospheric brightness temperatures, respectively, τ is the entire layer of atmospheric transmittance, E_p is the sea surface emissivity, T_{cold} is the effective cold space temperature, which is usually assumed to be a fixed value of 2.7 K, T_S is sea surface temperature, $T_{B\Omega}$ is the downwelling sky radiation that is scattered from the ocean surface, $R_p = 1 - E_p$ represents the sea surface reflectance, $\tau T_{B,scat,p}$ accounts for the atmosphere path length correction in the downwelling scattered sky radiation, and Ω_p represents an empirical correction factor for downwelling radiation that is reflected from nonspecular directions (Meissner and Wentz, 2009). Ω_p depends on the frequency f, incidence angle θ, transmittance τ and wind speed W.

3.2.1 *Sea surface emissivity model*

The sea surface emissivity model is the premise of this research. It is difficult to formulate a consistent theoretical model for the wind dependency on sea surface temperature (Stogryn, 1967; Hollinger, 1971). In this paper, the sea surface emissivity with nonspecular reflection is calculated from a sea surface emissivity model established by Meissner and Wentz (2012). The model can calculate the sea surface emissivity E_p for incidence

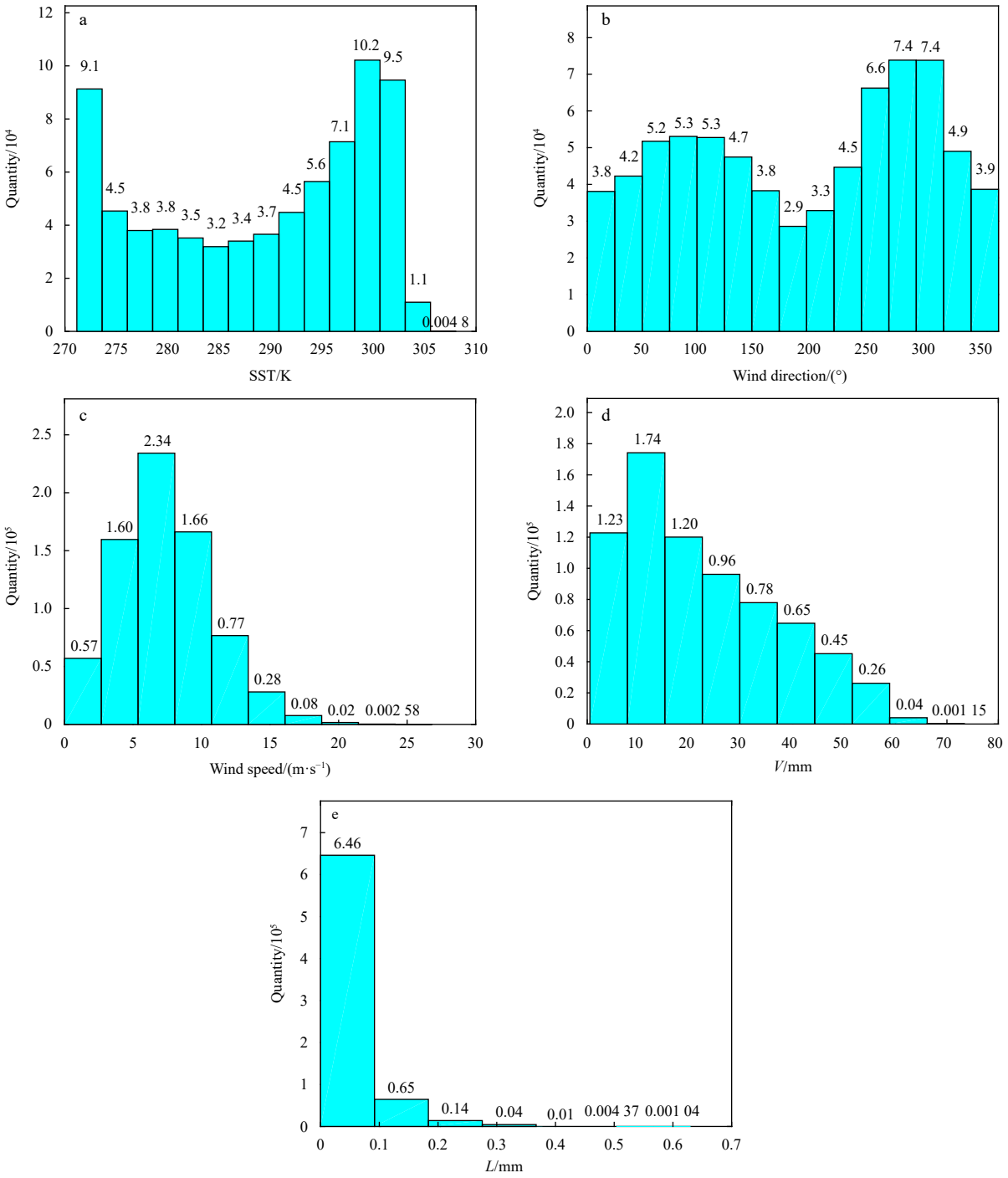

Fig. 3. Distribution histogram of environment parameters. a. Sea surface temperature, b. wind direction, c. wind speed, d. total column cloud water vapor content, and e. total column cloud liquid water content.

angles within the range of 0°–65° and sea surface temperature within the range of approximately –2°C to 40°C. This model divides the sea surface emissivity into three parts: the specular sea surface emissivity ($E_{0,\mathrm{p}}$), the emissivity increase caused by the wind speed W ($\Delta E_{W,\mathrm{p}}$), and the emissivity increase caused by the wind direction φ ($\Delta E_{\varphi,\mathrm{p}}$). The equation is as follows (Meissner and Wentz, 2012):

$$E_{\mathrm{p}} = E_{0,\mathrm{p}} + \Delta E_{W,\mathrm{p}} + \Delta E_{\varphi,\mathrm{p}}, \tag{5}$$

where $E_{0,\mathrm{p}}$ is by far the largest part, and it is a function of the frequency f, incidence angle θ, sea surface temperature T_{S} and salinity S. In addition, it is related to the complex permittivity of seawater ε. We calculate the complex permittivity of seawater using the algorithm established by Meissner and Wentz (2004), which is extensively validated and valid for fresh water and sea water in the temperature range of –2°C to 40°C and –2°C to 29°C, respectively. It was subsequently corrected in 2012 (Meissner and Wentz, 2004, 2012). The emissivity increase caused by the wind speed $\Delta E_{W,\mathrm{p}}$ is related to the wind speed W, and the increase in emissivity caused by the wind direction $\Delta E_{\varphi,\mathrm{p}}$ is related to the wind direction φ (Meissner and Wentz, 2012). The specific equa-

tion is not described in detail here.

3.2.2 *Atmospheric absorption model*

For atmosphere without rain where scattering can be neglected, there are three atmospheric absorption components in the microwave range of frequencies below 100 GHz: water vapor, liquid water and oxygen. The atmospheric parts T_{BU}, T_{BD} and τ in Eq. (5) can be calculated by an empirical model (Wentz and Meissner, 2000; Wang et al., 2005, 2014).

In this paper, we use an empirical model established by Wentz and Meissner (2000). This model needs to input frequency f, incidence angle θ, sea surface temperature T_{S}, total column cloud liquid water content L, and total column water vapor content V. The equations are not described in detail here.

However, the cloud liquid water absorption algorithm we used was developed by Wang et al. (2014) because the Wentz model (Wentz and Meissner, 2000) needs to input an average cloud temperature T_L, which is difficult to obtain. The equation is as follows:

$$A_L = a_{L0}(1 + a_{L1}V)L, \tag{6}$$

where a_{L0} and a_{L1} are empirical coefficients. In this paper, all the empirical coefficients are not listed here.

3.3 *Retrieval methods*

We use the filtered data to calculate the model brightness temperature $T_{\mathrm{B,mod}}$ with the radiation transmission forward model. The measured brightness temperature $T_{\mathrm{B,meas}}$ is simulated by adding Gaussian noises to the model brightness temperature $T_{\mathrm{B,mod}}$. The standard deviations of the Gaussian noises are 0.25 K, 0.50 K, and 0.75 K. In the absence of satellite observation data, it is a reasonable pre-research method used by many researchers (Bobylev et al., 2010).

Four retrieval algorithms for sea surface temperature retrieval from the measured temperature $T_{\mathrm{B,meas}}$ and incidence angle are developed. The algorithms are backpropagation neural network algorithm (BP), random forest algorithm (RF) and two multiple linear regression algorithms (RE1 and RE2) (Aires et al., 2001; Bobylev et al., 2010; Jung et al., 1998; Krasnopolsky et al., 2000). The four retrieval algorithms are all statistical methods. Each of them has its own advantages and disadvantages. BP has a strong nonlinear fitting ability. A three-layer neural network can approach any nonlinear problem infinitely. However, the gradient descent method is employed to train the network in BP; thus, local optimal solutions and gradient disappearances are easily produced. RF utilizes a bagging integration strategy based on decision tree-based learners and further introduces the selection of random attributes in the decision tree training process to enhance its generalization ability. RF can process multidimensional data with a faster calculation speed and no computational cost. Its anti-noise ability is strong, but overfitting occurs when the data are relatively noisy. The multiple linear regression algorithms (RE1 and RE2) are the simplest among all four algorithms. The two algorithms only need regression coefficients to retrieve sea surface temperature with $T_{\mathrm{B,meas}}$. However, the relationship between $T_{\mathrm{B,meas}}$ and sea surface temperature is not a simple linear relationship. A diagram of the process to retrieve sea surface temperature is shown in Fig. 4. It should be noted that the radiation transmission model is only used to calculate the model brightness temperature $T_{\mathrm{B,mod}}$, and it does not participate in the training of the retrieval algorithms.

We use a three-layer neural network, that is, the neural network contains a hidden layer. The number of hidden layer neurons is the same as that in the input layer. The model of the BP is shown in Fig. 5. There are 10 neurons in the input layer, which are incidence angle θ, measured brightness temperatures $T_{\mathrm{B,meas}}$ and bias; the output layer is sea surface temperature T_{S}. We use the sigmoid function as the activation function of the BP network. When training the RF, the inputs and output are the same as BP.

We use logarithmic regression and linear regression to retrieve sea surface temperature (Wentz and Meissner, 2000), which are called RE1 and RE2, respectively. RE1 and RE2 are performed at each incidence angle because the sensitivity of the brightness temperature to the incidence angle is very high. The generalized linear statistical regression algorithm is as follows:

$$T_{\mathrm{S}} = R\left(A_0 + \sum_{i=1}^{2\times n} A_i X(T_{\mathrm{B,meas},i})\right), \tag{7}$$

where T_{S} is the sea surface temperature, R and X are linearizing functions, n is the number of frequencies, and $T_{\mathrm{B,meas},i}$ is the measured brightness temperature. $R(Y) = Y$ is the linear function.

When fitting RE1,

$$X(T_{\mathrm{B}}) = T_{\mathrm{B}}, \quad f = 6.9 \text{ GHz and } 10.65 \text{ GHz}, \tag{8}$$

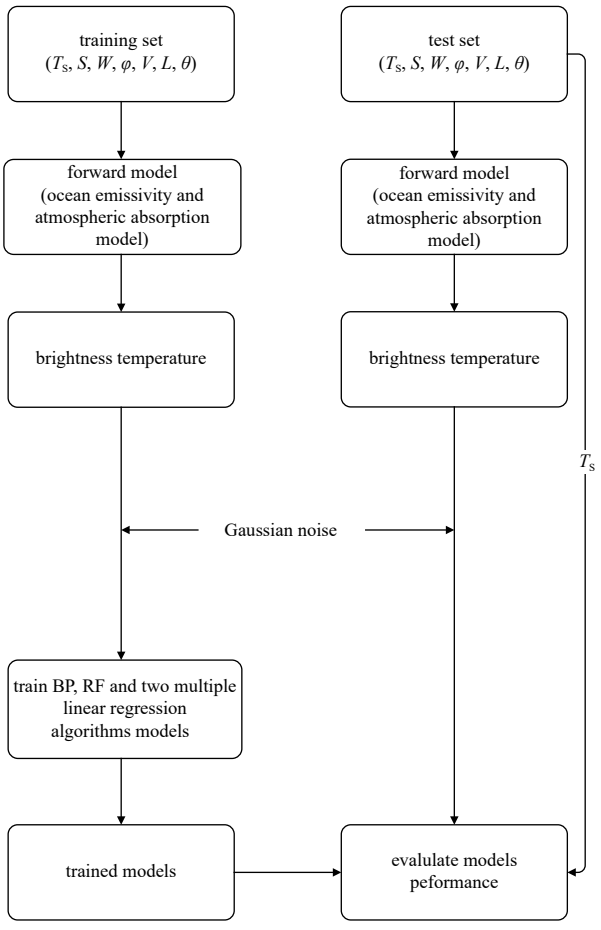

Fig. 4. Diagram of the process to retrieve sea surface temperature.

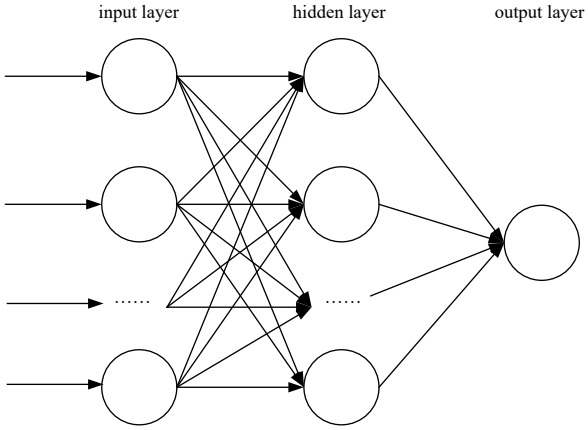

Fig. 5. Schematic diagram of the BP neural network.

$$X(T_{\mathrm{B}}) = -\ln(290 - T_{\mathrm{B}}), \quad f = 18.7\ \mathrm{GHz}\ \ \text{and}\ \ 23.8\ \mathrm{GHz}, \tag{9}$$

which is,

$$\begin{aligned} T_{\mathrm{S}} =& A_0 + A_1 T^{6.9}_{\mathrm{B,mean,v}} + A_2 T^{6.9}_{\mathrm{B,mean,h}} + A_3 T^{10.65}_{\mathrm{B,mean,v}} + \\ & A_4 T^{10.65}_{\mathrm{B,mean,h}} - A_5 \ln(290 - T^{18.7}_{\mathrm{B,mean,v}}) - \\ & A_6 \ln(290 - T^{18.7}_{\mathrm{B,mean,h}}) - A_7 \ln(290 - T^{23.8}_{\mathrm{B,mean,v}}) - \\ & A_8 \ln(290 - T^{23.8}_{\mathrm{B,mean,h}}), \end{aligned} \tag{10}$$

when fitting RE2,

$$X(T_{\mathrm{B}}) = T_{\mathrm{B}},\ f = 6.9\ \mathrm{GHz}, \ 10.65\ \mathrm{GHz}, \ 18.7\ \mathrm{GHz}\ \ \text{and}\ \ 23.8\ \mathrm{GHz}, \tag{11}$$

which is,

$$\begin{aligned} T_{\mathrm{S}} =& A_0 + A_1 T^{6.9}_{\mathrm{B,mean,v}} + A_2 T^{6.9}_{\mathrm{B,mean,h}} + A_3 T^{10.65}_{\mathrm{B,mean,v}} + \\ & A_4 T^{10.65}_{\mathrm{B,mean,h}} + A_5 T^{18.7}_{\mathrm{B,mean,v}} + A_6 T^{18.7}_{\mathrm{B,mean,h}} + \\ & A_7 T^{23.8}_{\mathrm{B,mean,v}} + A_8 T^{23.8}_{\mathrm{B,mean,h}}. \end{aligned} \tag{12}$$

It should be noted that the radiation transmission forward model can calculate radiation in the range of $0^\circ \leqslant \theta \leqslant 65^\circ$. In this paper, we study the sea surface temperature retrieval in the range of $0^\circ \leqslant \theta \leqslant 65^\circ$ though the incidence angle range of the one-dimensional synthetic aperture microwave radiometer is $0^\circ \leqslant \theta \leqslant 51^\circ$.

4 Results and discussion

4.1 *Sensitivity of brightness temperature to sea surface temperature*

The sensitivity to sea surface temperature determines the retrieval precision at different incidence angles. We assumed a environment scene to research the sensitivity of the brightness temperature to the sea surface temperature, which are shown in Table 2. The sea surface temperature is set range from 273.15 K to 313.15 K, and other parameters are set as constants. We calculated the sensitivity to sea surface temperature at different incidence angles; the equation is as follows:

$$\mathrm{SE} = \frac{1}{n}\sum_{i=1}^{n} \frac{\partial T_{\mathrm{B,mod,p}}}{\partial T_{\mathrm{S},i}}, \tag{13}$$

where SE is the sensitivity of the brightness temperature to the sea surface temperature. n is the number of the sea surface temperature T_{S}, and $T_{\mathrm{B,mod,p}}$ is the model brightness temperature.

Table 2. Geophysical parameter values for the background field used in the sensitivity analysis

Scene	S	T_{S}/K	W/(m·s^{-1})	φ/(°)	V/mm	L/mm
Scene2	35	273.15–313.15	15	30	30	0.1

Figure 6 shows the relationship between the sensitivity of the vertical and horizontal polarization brightness temperature to the sea surface temperature and incidence angle. It can be observed that 6.9 GHz provides the best sensitivity, with the consequence that 6.9 GHz has the greatest influence on retrieval precision. The sensitivity to the sea surface temperature is higher at vertical polarization than at horizontal polarization. The sensitivity to sea surface temperature increases with incidence angle at vertical polarization, with the result that vertical polarization increases the retrieval precision at a larger incidence angle. At horizontal polarization of 6.9 GHz and 10.65 GHz, the sensitivity of to the sea surface temperature decreases with the incidence angle. Its influence is the opposite of vertical polarization. However, at 18.7 GHz and 23.8 GHz, the sensitivity of horizontal polarization is almost constant. Figure 7 shows the trend of sensitivity with sea surface temperature at $\theta = 30^\circ$.

4.2 *Experiment results*

There are two major problems that make the one-dimensional synthetic aperture microwave radiometer determination of sea surface temperature a substantial challenge: the calibration error and modeling error. For convenience, we assume that the forward model is accurate. The calibration error can be regarded as random noise. Therefore, we add Gaussian noise to the model brightness temperature.

To improve the reliability of error statistics, we compute the root mean square (RMS) error and bias:

$$\sigma = \sqrt{\frac{1}{N}\sum_{k=1}^{N}(T^{\mathrm{true}}_{\mathrm{S},k} - T_{\mathrm{S},k})^2}, \tag{14}$$

$$B = \frac{1}{N}\sum_{k=1}^{N}(T^{\mathrm{true}}_{\mathrm{S},k} - T_{\mathrm{S},k}), \tag{15}$$

where σ is the RMS error of T_{S}, N is the number of T_{S}, and $T^{\mathrm{true}}_{\mathrm{S}}$ is true value of T_{S}. B is the mean bias of T_{S}.

4.2.1 *Influence of the noise and the incidence angle on the retrieval result*

Figure 8 illustrates the relationships between the RMS error and the mean bias of the four retrieval algorithms and incidence angle. The bold dotted lines, thin dotted lines and dashed lines are the retrieval results with added noises of 0.25 K, 0.50 K, and 0.75 K, respectively. In Fig. 8, the training set results are on the left, and the test set results are on the right. The results of the training set and test set have few differences.

The RMS errors increase with the Gaussian noise increasing, which means that the more accurate the one-dimensional synthetic aperture microwave radiometer measure is, the more accurate the retrieval of the sea surface temperature. In addition to RF, the RMS error differences between dashed lines (0.75 K) and thin dotted lines (0.50 K) are larger than those between thin

dotted lines (0.50 K) and bold dotted lines (0.25 K). The effect of the Gaussian noise on the RMS error is different at different incidence angles. In general, it is larger at $0° \leqslant \theta \leqslant 20°$ than at $\theta > 20°$. In contrast, the effect of the Gaussian noise on the mean bias is small. The mean bias fluctuates around approximately 0 K with the incidence angel.

From Figs 8i, j, m and n, we can see that the RMS error first decreases with the incidence angle in the range of $0° \leqslant \theta \leqslant 55°$

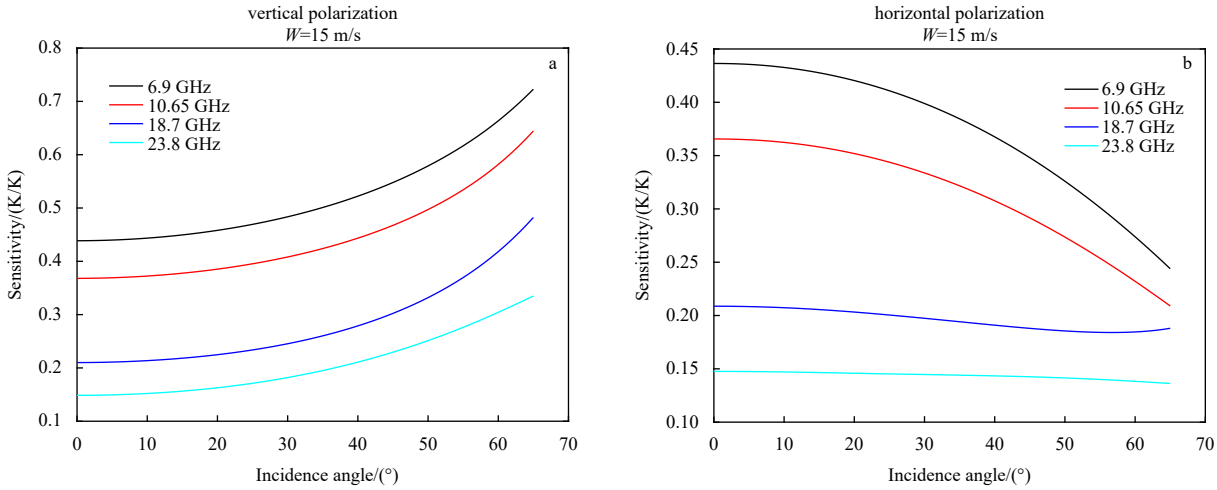

Fig. 6. The relationship between sensitivity of brightness temperature to SST and incidence angle.

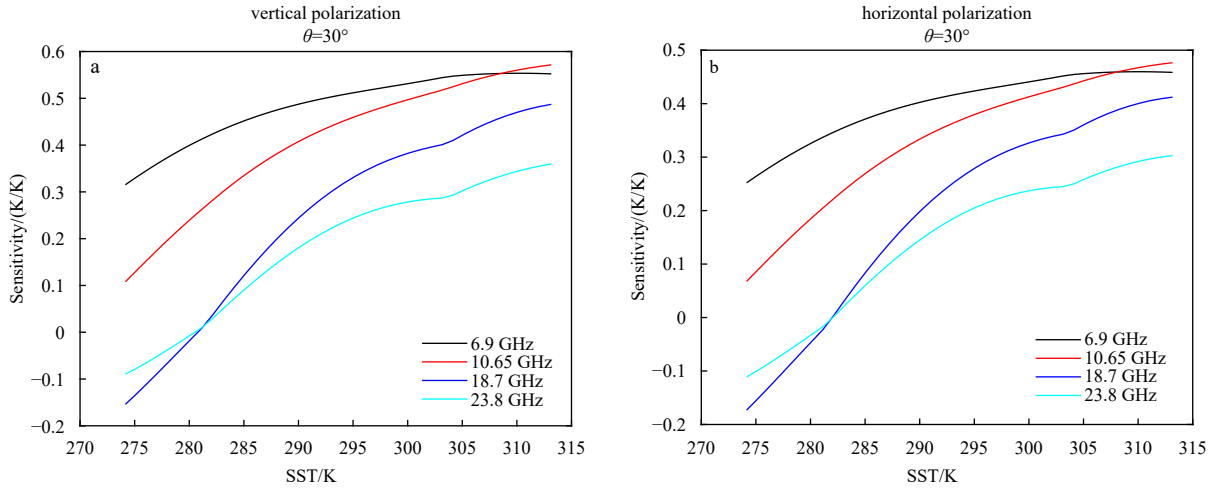

Fig. 7. The relationship between sensitivity of brightness temperature to SST and SST at $\theta = 30°$.

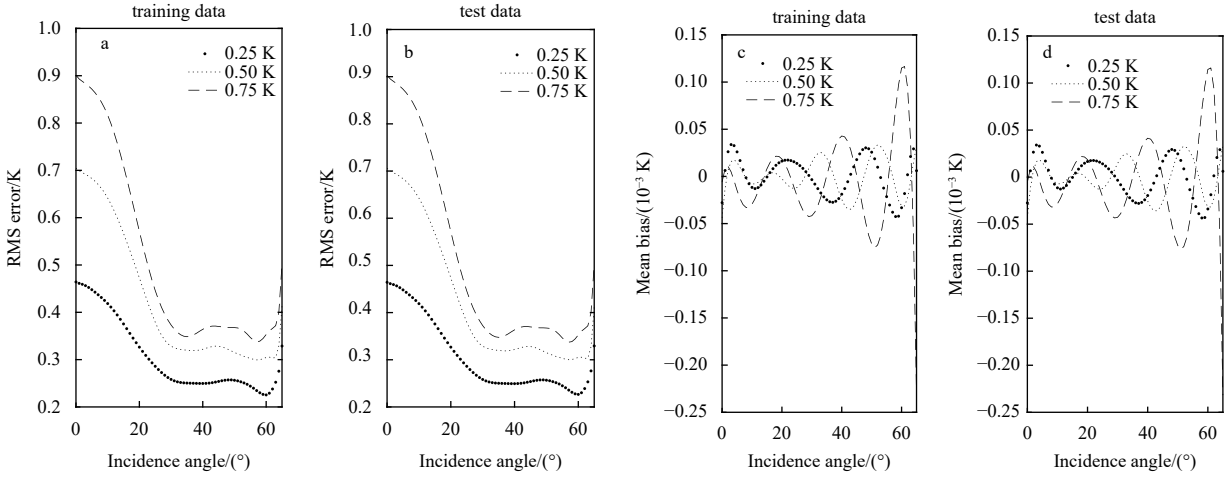

Fig. 8.

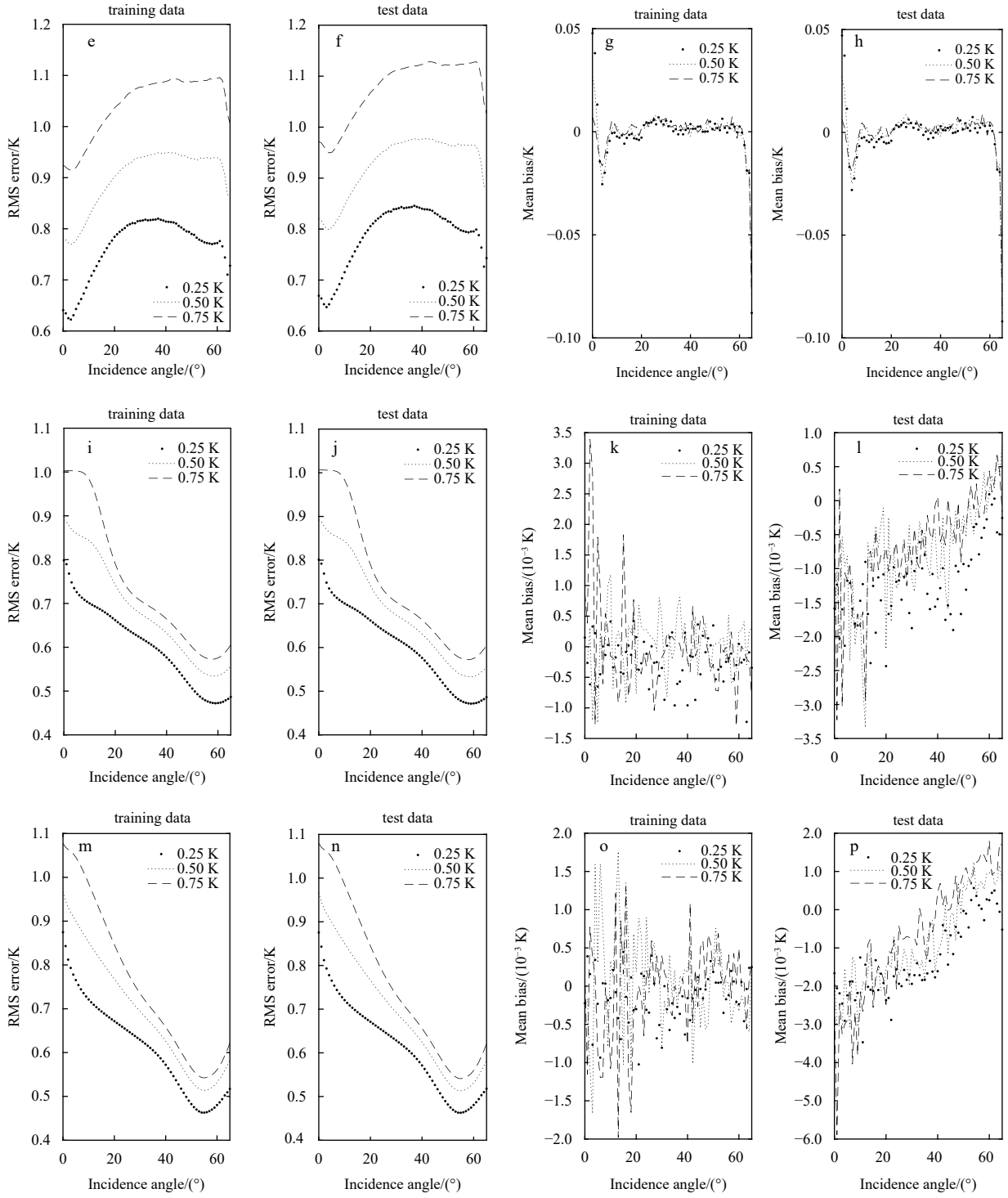

Fig. 8. Relationships between the RMS error and the mean bias and incidence angle. a–d. The trend of the RMS error and the mean bias of BP with the incidence angle; e–h. the trend of the RMS error and the mean bias of RF with the incidence angle; i–l. the trend of the RMS error and the mean bias of RE1 with the incidence angle; m–p. the trend of the RMS error and the mean bias of RE2 with the incidence angle.

and then increases in the range of $55° \leqslant \theta \leqslant 65°$. This trend in Figs 8i, j, m and n can be explained by the sensitivity to the sea surface temperature (Fig. 6). We find that the reason for the RMS error reaching the minimum at $\theta_{EIA} \approx 55°$ is affected by the horizontal polarization brightness temperature of 6.9 GHz and 10.65 GHz. The minimum of the RMS error in Figs 8i, j, m and n will occur at $\theta = 65°$ when we retrieve the sea surface temperature without 6.9 GHz and 10.65 GHz horizontal polarization brightness temperature. Therefore, we conclude that the horizontal polarization brightness temperature of 6.9 GHz and 10.65 GHz has a greater effect on the large incidence angles. In contrast, the vertical polarization has a greater effect on the low incidence angles.

The relationship between the RMS error and the incidence

angle in Figs 8a, b, i and j are similar because the principles of BP and RE are similar. BP updates weights through error back propagation, and RE obtains the regression coefficients through fitting. However, BP presents higher retrieval precision than RE1 and RE2. In general, the RMS error of BP, RE1 and RE2 are consistent with the sensitivity to the sea surface temperature to some extent. In contrast, the RMS error of RF is the opposite of other algorithms.

Tables 3 and 4 show the average RMS errors and mean biases, respectively, that is, the average of the retrieval result at all incidence angles. The top values are the training set, while the bottom values are the test set. Table 3 shows that the RF has the largest retrieval errors, whereas the BP has the smallest retrieval errors (its accuracy is approximately twice that of the BP). The retrieval errors of the RE1 and RE2 are mostly the same. As shown in Table 4, the average mean biases of the four algorithms are very low.

4.2.2 *Influence of sea surface temperature on the retrieval errors*

To research the relationship between the four algorithms' retrieval accuracy and sea surface temperature, this section analyzes the retrieval errors with a noise of 0.50 K and $\theta=30°$ from Section 4.1. We divide the sea surface temperature into 10 intervals and calculate the RMS error and mean bias for each temperature interval, as shown in Fig. 9. The scatterplots of the retrieval sea surface temperature and true sea surface temperature are shown in Fig. 10. Tables 5 and 6 list the sample size N, the RMS error and mean bias of each temperature interval in the training set and test set, respectively.

As seen from Fig. 9, Tables 5 and 6, although the temperature interval and samples size slightly differ between the training set and the test set, the differences between the RMS errors and mean biases of them are small. The following describes the main results for the training set. Table 5 shows that there are only 154 data points in the interval of 304.34–308.02 K, but the RMS error of BP is only 0.36 K. This confirms that the BP is less affected by the sample size. In addition, the curve of BP in Figs 9c and d is consistently stable at approximately 0 K.

The retrieval errors of RE1 and RE2 are similar. The RMS error and mean bias are the largest in the temperature range with the smallest sample size, with the consequence that the sample size has a considerable influence on the retrieval precision in multiple linear regression. The curves of RE1 and RE2 in Figs 9c and d first decrease and then increase. In addition, at most temperature intervals, the absolute value of the mean bias exceeds half of the RMS error.

Compared with the other algorithms, the RF has the highest retrieval error. The RMS error is the largest at each temperature interval (much larger than the RMS error of the BP). The mean bias of the RF is small relative to the RMS error in the sea surface temperature range from 271.15 K to 300.65 K, which indicates that the retrieval sea surface temperature evenly distributes around the true value in this sea surface range. However, the RF performs poorly in the sea surface temperature range from 300.66 K to 308.02 K, and this can be seen in Figs 10c and d. We conclude that the sample size has a substantial influence on the RF retrieval accuracy. Compared with the other three algorithms, RF is not suitable for retrieving sea surface temperature with the one-dimensional synthetic aperture microwave radiometer.

5 Conclusions

In this paper, a one-dimensional synthetic aperture microwave radiometer is proposed to retrieve sea surface temperature from space. We assume that the spaceborne one-dimensional synthetic aperture microwave radiometer is operating at an or-

Table 3. Mean RMS errors, where the top values are the training set and the bottom values are the test set

Noise/K	Mean RMS error/K			
	BP	RF	RE1	RE2
0.25	0.30	0.76	0.60	0.61
	0.30	0.78	0.60	0.61
0.50	0.42	0.90	0.68	0.69
	0.42	0.92	0.68	0.68
0.75	0.50	1.04	0.74	0.75
	0.51	1.07	0.74	0.75

Table 4. The average mean biases, where the top values are the training set and the bottom values are the test set

Noise/K	Mean bias/K			
	BP	RF	RE1	RE2
0.25	-1.0×10^{-4}	-6.0×10^{-4}	2.1×10^{-4}	-1.5×10^{-4}
	-1.1×10^{-4}	−0.001	-1.2×10^{-3}	-1.3×10^{-3}
0.50	-3.7×10^{-4}	-6.0×10^{-4}	-3.2×10^{-5}	7.1×10^{-5}
	-5.7×10^{-4}	-4.7×10^{-4}	-7.7×10^{-4}	-8.9×10^{-4}
0.75	−0.005	-5.4×10^{-4}	-1.2×10^{-5}	-2.6×10^{-5}
	−0.005	-6.4×10^{-4}	6.6×10^{-4}	-6.6×10^{-4}

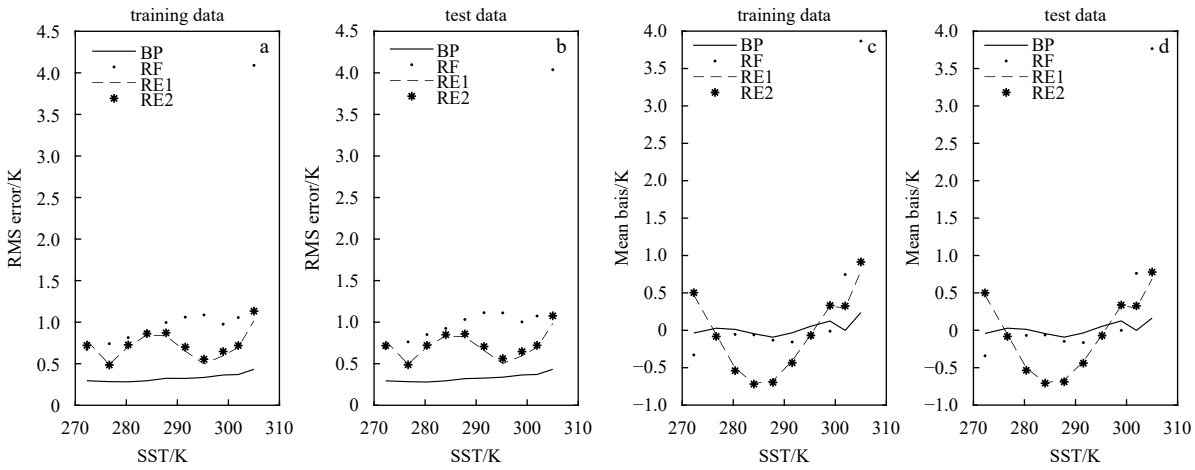

Fig. 9. Relationships between the retrieval errors and sea surface temperature when the added noise is 0.50 K and $\theta=30°$.

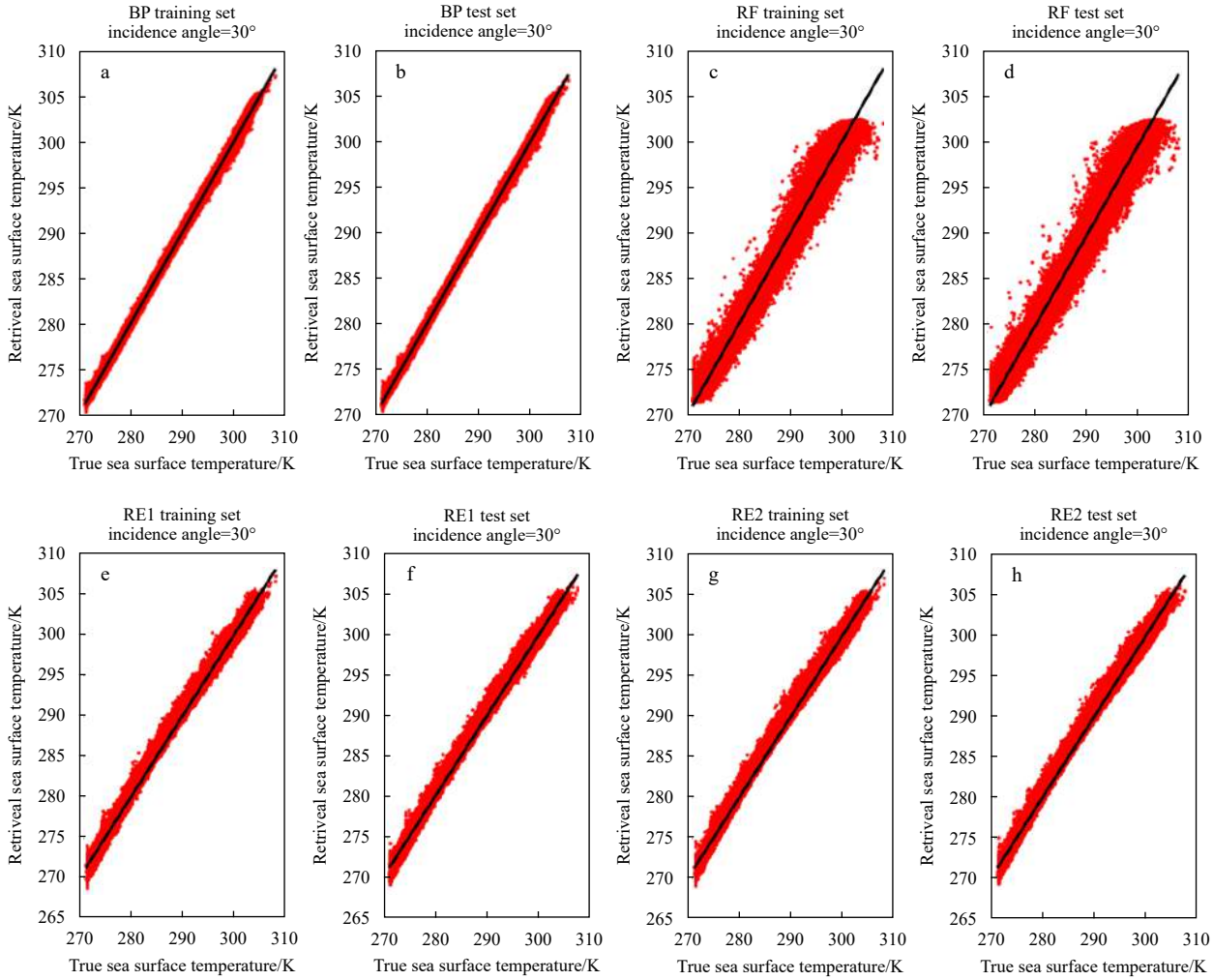

Fig. 10. Scatterplots of retrieval sea surface temperature and true sea surface temperature for Gaussian error of 0.5 K and $\theta = 30°$.

Table 5. SST interval and sample size for each interval in the training set and the corresponding RMS error and mean bias

SST/K	*N*	RMS error and mean bias/K			
		BP	RF	RE1	RE2
271.15–274.84	58 459	0.29/−0.03	0.67/−0.32	0.77/0.47	0.72/0.50
274.85–278.53	29 087	0.28/0.02	0.74/−0.09	0.49/−0.05	0.48/−0.08
278.54–282.21	28 518	0.28/0.01	0.81/−0.05	0.70/−0.50	0.72/−0.53
282.22–285.90	24 194	0.29/−0.04	0.89/−0.06	0.84/−0.71	0.86/−0.71
285.91–289.59	25 850	0.32/−0.09	0.99/−0.13	0.83/−0.67	0.87/−0.69
289.60–293.27	31 802	0.32/−0.03	1.06/−0.15	0.65/−0.40	0.70/−0.43
293.28–296.96	44 625	0.33/0.05	1.08/−0.09	0.49/−0.05	0.55/−0.06
296.97–300.65	70 249	0.36/0.10	0.97/−0.01	0.59/0.32	0.64/0.33
300.66–304.33	52 658	0.37/0.001	1.05/0.74	0.66/0.29	0.71/0.32
304.34–308.02	154	0.36/0.20	4.09/3.86	1.01/0.79	1.13/0.91
All	365 624	0.38/−0.01	0.93/0.004	0.67/0.00	0.69/0.00

Note: The RMS error and the mean bias are separated by "/".

bital height of 900 km and the antenna elements of all frequencies have the same spatial resolution. First, we use the ERA5 reanalysis data to calculate the model brightness temperature with the radiation transmission forward model. The measured brightness temperature is simulated by adding different Gaussian noises to the model brightness temperature. Then, the BP neural network, RF algorithm and multiple linear regression algorithms (RE1 and RE2) are used to retrieve sea surface temperature within the incidence angle range from 0° to 65°. The main conclusions are as follows:

The sensitivity of all frequencies to sea surface temperature increases with the incidence angle at the vertical polarization. At the horizontal polarization of 6.9 GHz and 10.65 GHz, the sensitivity to sea surface temperature decreases with the incidence angle. However, at 18.7 GHz and 23.8 GHz, the sensitivity of the horizontal polarization to the sea surface temperature is almost

Table 6. SST interval and sample size for each interval in the test set and the corresponding RMS error and mean bias

SST/K	N	RMS error and mean bias/K			
		BP	RF	RE1	RE2
271.15–274.84	58 001	0.29/−0.04	0.69/−0.34	0.78/0.47	0.72/0.50
274.85–278.53	29 091	0.28/0.03	0.76/−0.09	0.49/−0.06	0.49/−0.08
278.54–282.21	28 662	0.28/0.01	0.85/−0.07	0.70/−0.50	0.72/−0.53
282.22–285.90	24 139	0.29/−0.04	0.92/−0.06	0.84/−0.70	0.85/−0.71
285.91–289.59	25 993	0.32/−0.09	1.03/−0.15	0.82/−0.67	0.86/−0.69
289.60–293.27	31 739	0.33/−0.03	1.11/−0.16	0.66/−0.41	0.71/−0.44
293.28–296.96	44 534	0.34/0.05	1.11/−0.09	0.50/−0.06	0.56/−0.07
296.97–300.65	70 595	0.36/0.13	1.01/0.00	0.59/0.33	0.65/0.34
300.66–304.33	52 703	0.37/0.00	1.07/0.76	0.70/0.30	0.72/0.33
304.34–308.02	167	0.43/0.16	4.03/3.76	0.98/0.69	1.07/0.78
All	365 624	0.39/−0.01	0.97/0.004	0.67/0.00	0.69/−0.001

Note: The RMS error and the mean bias are separated by "/".

constant.

The RMS errors increase with the Gaussian noise increase. The effect of the Gaussian noise on the RMS error is larger at $0^\circ \leqslant \theta \leqslant 20^\circ$ than at $\theta > 20^\circ$. In contrast, the effect of the Gaussian noise on the mean bias is small. The mean bias fluctuates around approximately 0 K with the incidence angel.

The RMS error of RE1 and RE2 decreases first and then increases with the incidence angle and reaches the minimum at $\theta \approx 55^\circ$. The reason is that the influence of horizontal polarization signals of 6.9 GHz and 10.65 GHz on the retrieval precision increases with the incidence angle, and the sensitivity of the horizontal polarization of 6.9 GHz and 10.65 GHz to sea surface temperature decreases with the incidence angle.

The BP boasts the smallest retrieval errors, while the RF has the largest retrieval errors. Furthermore, the sample size has little effect on the BP retrieval precision. To a certain degree, for example, even if there are only 154 data points, the BP can obtain a sufficiently low retrieval error of 0.36 K. However, the sample size has a great influence on the RF, RE1 and RE2. In particular, the RMS error of the RF reaches 4.09 K with a sample size of 154. Although the BP is an older model, it is most suitable for retrieving sea surface temperature by a spaceborne one-dimensional synthetic aperture microwave radiometer.

The research in this paper provides a reference for sea surface temperature retrieval by a spaceborne one-dimensional synthetic aperture microwave radiometer. However, our findings are based on clear-sky conditions. In the future, we will work on sea surface temperature retrieval under precipitation conditions.

References

Aires F, Prigent C, Rossow W B, et al. 2001. A new neural network approach including first guess for retrieval of atmospheric water vapor, cloud liquid water path, surface temperature, and emissivities over land from satellite microwave observations. Journal of Geophysical Research, 106(D4): 14887–14907

Alsweiss S O, Jelenak Z, Chang P S. 2017. Remote sensing of sea surface temperature using AMSR-2 measurements. IEEE Journal of Selected Topics in Applied Earth Observations & Remote Sensing, 10(9): 3948–3954

Bettenhausen M H, Smith C K, Bevilacqua R M, et al. 2006. A nonlinear optimization algorithm for WindSat wind vector retrievals. IEEE Transactions on Geoscience and Remote Sensing, 44(3): 597–610, doi: 10.1109/TGRS.2005.862504

Bobylev L P, Zabolotskikh E V, Mitnik L M, et al. 2010. Atmospheric water vapor and cloud liquid water retrieval over the Arctic ocean using satellite passive microwave sensing. IEEE Transactions on Geoscience and Remote Sensing, 48(1): 283–294, doi: 10.1109/TGRS.2009.2028018

Brown S T, Ruf C S, Lyzenga D R. 2006. An emissivity-based wind vector retrieval algorithm for the WindSat polarimetric radiometer. IEEE Transactions on Geoscience and Remote Sensing, 44(3): 611–621, doi: 10.1109/TGRS.2005.859351

Camps A, Park H, Bandeiras J, et al. 2016. Microwave imaging radiometers by aperture synthesis—Performance simulator (Part 1): Radiative transfer module. Journal of Imaging, 2(2): 17, doi: 10.3390/jimaging2020017

Chelton D B, Wentz F J. 2005. Global microwave satellite observations of sea surface temperature for numerical weather prediction and climate research. Bulletin of the American Meteorological Society, 86(8): 1097–1116, doi: 10.1175/BAMS-86-8-1097

Corbella I, Duffo N, Vall-Llossera M, et al. 2004. The visibility function in interferometric aperture synthesis radiometry. IEEE Transactions on Geoscience and Remote Sensing, 42(8): 1677–1682, doi: 10.1109/TGRS.2004.830641

Emanuel A K. 1999. Thermodynamic control of hurricane intensity. Nature, 401(6754): 665–669, doi: 10.1038/44326

Goodberlet M A, Swift C T, Wilkerson J C. 1990. Ocean surface wind speed measurements of the special sensor microwave/imager (SSM/I). IEEE Transactions on Geoscience and Remote Sensing, 28(5): 823–828, doi: 10.1109/36.58969

Hollinger J P. 1971. Passive microwave measurements of sea surface roughness. IEEE Transactions on Geoscience Electronics, 9(3): 165–169, doi: 10.1109/TGE.1971.271489

Jung T, Ruprecht E, Wagner F. 1998. Determination of cloud liquid water path over the oceans from special sensor microwave/imager (SSM/I) data using neural networks. Journal of Applied Meteorology and Climatology, 37(8): 832–844, doi: 10.1175/1520-0450(1998)037<0832:DOCLWP>2.0.CO;2

Kilic L, Prigent C, Aires F, et al. 2018. Expected performances of the copernicus imaging microwave radiometer (CIMR) for an all-weather and high spatial resolution estimation of ocean and sea ice parameters. Journal of Geophysical Research: Oceans, 123(10): 7564–7580, doi: 10.1029/2018JC014408

Koner P K, Harris A, Maturi E. 2015. A physical deterministic inverse method for operational satellite remote sensing: An application for sea surfacetemperature retrievals. IEEE Transactions on Geoscience and Remote Sensing, 53(11): 5872–5888, doi: 10.1109/TGRS.2015.2424219

Krasnopolsky V M, Gemmill W H, Breaker L C. 2000. A neural network multiparameter algorithm for SSM/I ocean retrievals: Comparisons and validations. Remote Sensing of Environment, 73(2): 133–142, doi: 10.1016/S0034-4257(00)00088-2

Le Vine D M. 1990. The sensitivity of synthetic aperture radiometers for remote sensing applications from space. Radio Science, 25(4): 441–453, doi: 10.1029/RS025i004p00441

Le Vine D M, Griffis A J, Swift C T, et al. 1994. ESTAR: A synthetic aperture microwave radiometer for remote sensing applications. Proceedings of the IEEE, 82(12): 1787–1801, doi: 10.1109/5.338071

Le Vine D M, Kao M, Swift C T, et al. 1990. Initial results in the devel-

opment of a synthetic aperture microwave radiometer. IEEE Transactions on Geoscience and Remote Sensing, 28(4): 614–619, doi: 10.1109/TGRS.1990.572965

Le Vine D M, Swift C T, Haken M. 2001. Development of the synthetic aperture microwave radiometer, ESTAR. IEEE Transactions on Geoscience and Remote Sensing, 39(1): 199–202, doi: 10.1109/36.898685

Lim B H. 2009. The design and development of a geostationary synthetic thinned aperture radiometer [dissertation]. Michigan: The University of Michigan

Martin-Neira M, Menard Y, Goutoule J M, et al. 1994. MIRAS, a two-dimensional aperture synthesis radiometer. In: Proceeding of the 1994 IEEE International Geoscience and Remote Sensing Symposium. Pasadena, CA, USA: IEEE, 1323-1325

Martin-Neira M, Ribo S, Martin-Polegre A J. 2002. Polarimetric mode of MIRAS. IEEE Transactions on Geoscience and Remote Sensing, 40(8): 1755–1768, doi: 10.1109/TGRS.2002.802489

Mätzler C. 2006. Thermal Microwave Radiation: Applications for Remote Sensing. London: The Institution of Engineering and Technology

McClain E P, Pichel W G, Walton C C. 1985. Comparative performance of AVHRR-based multichannel sea surface temperatures. Journal of Geophysical Research: Oceans, 90(C6): 11587–11601, doi: 10.1029/JC090iC06p11587

McPhaden M J. 1999. Genesis and evolution of the 1997–98 El Niño. Science, 283(5404): 950–954, doi: 10.1126/science.283.5404.950

Meissner T, Wentz F J. 2004. The complex dielectric constant of pure and sea water from microwave satellite observations. IEEE Transactions on Geoscience and Remote Sensing, 42(9): 1836–1849, doi: 10.1109/TGRS.2004.831888

Meissner T, Wentz F. 2005. Ocean retrievals for WindSat: Radiative transfer model, algorithm, validation. In: Proceedings of OCEANS 2005 MTS/IEEE. Washington, DC, USA: IEEE, 130–133

Meissner T, Wentz F J. 2009. Wind-vector retrievals under rain with passive satellite microwave radiometers. IEEE Transactions on Geoscience and Remote Sensing, 47(9): 3065–3083, doi: 10.1109/TGRS.2009.2027012

Meissner T, Wentz F J. 2012. The emissivity of the ocean surface between 6 and 90 GHz over a large range of wind speeds and earth incidence angles. IEEE Transactions on Geoscience and Remote Sensing, 50(8): 3004–3026, doi: 10.1109/TGRS.2011.2179662

Obligis E, Labroue S, Amar A, et al. 2005. Neural networks to retrieve sea surface salinity from SMOS brightness temperatures. In: Proceedings of the 2005 IEEE International Geoscience and Remote Sensing Symposium. Seoul, South Korea: IEEE, 2568–2571

Ruf C S, Swift C T, Tanner A B, et al. 1988. Interferometric synthetic aperture microwave radiometry for the remote sensing of the earth. IEEE Transactions on Geoscience and Remote Sensing, 26(5): 597–611, doi: 10.1109/36.7685

Schanda E. 1979. Multiple wavelength aperture synthesis for passive sensing of the earth's surface. In: 1979 Antennas and Propagation Society International Symposium. Seattle, WA, USA: IEEE, 762–763

Stogryn A. 1967. The apparent temperature of the sea at microwave frequencies. IEEE Transactions on Antennas and Propagation, 15(2): 278–286, doi: 10.1109/TAP.1967.1138900

Ulaby F T, Dobson M C, Brunfeldt D R. 1983. Improvement of moisture estimation accuracy of vegetation-covered soil by combined active/passive microwave remote sensing. IEEE Transactions on Geoscience and Remote Sensing, GE-21(3): 300–307, doi: 10.1109/TGRS.1983.350557

Wang Rui, Shi Shunwen, Yan Wei, et al. 2014. Sea surface wind retrieval from polarimetric microwave radiometer in typhoon area. Chinese Journal of Geophysics (in Chinese), 57(3): 738–751

Wang Naiyu, Chang P S, Bettenhausen M, et al. 2005. WindSat physically based forward model: atmospheric component. In: Proceedings of SPIE—The International Society for Optical Engineering, vol. 5656, Active and Passive Remote Sensing of the Oceans: 104–110, doi: 10.1117/12.578811

Wentz F J, Meissner T. 2000. Algorithm theoretical basis document (ATBD). Version 2: AMSR Ocean Algorithm. Santa Rosa, CA: Remote Sensing Systems